Structural and functional analysis of a potent sarbecovirus neutralizing antibody

Dora Pinto[1,7], Young-Jun Park[2,7], Martina Beltramello[1,7], Alexandra C. Walls[2,7], M. Alejandra Tortorici[2,3], Siro Bianchi[1], Stefano Jaconi[1], Katja Culap[1], Fabrizia Zatta[1], Anna De Marco[1], Alessia Peter[1], Barbara Guarino[1], Roberto Spreafico[4], Elisabetta Cameroni[1], James Brett Case[6], Rita E. Chen[6], Colin Havenar-Daughton[4], Gyorgy Snell[4], Amalio Telenti[4], Herbert W. Virgin[4], Antonio Lanzavecchia[1,5], Michael S. Diamond[6], Katja Fink[1], David Veesler[2*] and Davide Corti[1*]

[1] Humabs Biomed SA, a subsidiary of Vir Biotechnology, 6500 Bellinzona, Switzerland.
[2] Department of Biochemistry, University of Washington, Seattle, Washington 98195, USA.
[3] Institut Pasteur & CNRS UMR 3569, Unité de Virologie Structurale, 75015, Paris, France.
[4] Vir Biotechnology, San Francisco, California 94158, USA
[5] Institute for Research in Biomedicine, Università della Svizzera Italiana, 6500 Bellinzona, Switzerland.
[6] Departments of Medicine, Molecular Microbiology, Pathology & Immunology, Washington University School of Medicine, St. Louis, MO 631110, USA
[7] These authors contributed equally

Correspondence: dveesler@uw.edu, dcorti@vir.bio

SARS-CoV-2 is a newly emerged coronavirus responsible for the current COVID-19 pandemic that has resulted in more than one million infections and 73,000 deaths[1,2]. Vaccine and therapeutic discovery efforts are paramount to curb the pandemic spread of this zoonotic virus. The SARS-CoV-2 spike (S) glycoprotein promotes entry into host cells and is the main target of neutralizing antibodies. Here we describe multiple monoclonal antibodies targeting SARS-CoV-2 S identified from memory B cells of a SARS survivor infected in 2003. One antibody, named S309, potently neutralizes SARS-CoV-2 and SARS-CoV pseudoviruses as well as authentic SARS-CoV-2 by engaging the S receptor-binding domain. Using cryo-electron microscopy and binding assays, we show that S309 recognizes a glycan-containing epitope that is conserved within the sarbecovirus subgenus, without competing with receptor attachment. Antibody cocktails including S309 along with other antibodies identified here further enhanced SARS-CoV-2 neutralization and may limit the emergence of neutralization-escape mutants. These results pave the way for using S309 and S309-containing antibody cocktails for prophylaxis in individuals at high risk of exposure or as a post-exposure therapy to limit or treat severe disease.

41 Coronavirus entry into host cells is mediated by the transmembrane spike (S)
42 glycoprotein that forms homotrimers protruding from the viral surface[3]. The S
43 glycoprotein comprises two functional subunits: S_1 (divided into A, B, C and D domains)
44 that is responsible for binding to host cell receptors and S_2 that promotes fusion of the
45 viral and cellular membranes[4,5]. Both SARS-CoV-2 and SARS-CoV belong to the
46 sarbecovirus subgenus and their S glycoproteins share 80% amino acid sequence
47 identity[6]. SARS-CoV-2 S is closely related to the bat SARS-related CoV (SARSr-CoV)
48 RaTG13 with which it shares 97.2% amino acid sequence identity[1]. We and others
49 recently demonstrated that human angiotensin converting enzyme 2 (hACE2) is a
50 functional receptor for SARS-CoV-2, as is the case for SARS-CoV[1,6-8]. The S domain
51 B (S^B) is the receptor binding domain (RBD) and binds to hACE2 with high-affinity,
52 possibly contributing to the current rapid SARS-CoV-2 transmission in humans[6,9], as
53 previously proposed for SARS-CoV[10].
54 As the coronavirus S glycoprotein mediates entry into host cells, it is the main
55 target of neutralizing antibodies and the focus of therapeutic and vaccine design
56 efforts[3]. The S trimers are extensively decorated with N-linked glycans that are
57 important for protein folding[11] and modulate accessibility to host proteases and
58 neutralizing antibodies[12-15]. Cryo-electron microscopy (cryoEM) structures of SARS-
59 CoV-2 S in two distinct functional states[6,9] along with cryoEM and crystal structures of
60 SARS-CoV-2 S^B in complex with hACE2[16-18] revealed dynamic states of S^B domains,
61 providing a blueprint for the design of vaccines and inhibitors of viral entry.
62 Passive administration of monoclonal antibodies (mAbs) could have a major
63 impact on controlling the SARS-CoV-2 pandemic by providing immediate protection,
64 complementing the development of prophylactic vaccines. Accelerated development
65 of mAbs in a pandemic setting could be reduced to 5-6 months compared to the
66 traditional timeline of 10-12 months (Kelley B., Developing monoclonal antibodies at
67 pandemic speed, Nat Biotechnol, in press). The recent finding that ansuvimab
68 (mAb114) is a safe and effective treatment for symptomatic Ebola virus infection is a
69 striking example of the successful use of mAb therapy during an infectious disease
70 outbreak[19,20]. We previously isolated potently neutralizing human mAbs from memory
71 B cells of individuals infected with SARS-CoV[21] or MERS-CoV[22]. Passive transfer of
72 these mAbs protected animals challenged with various SARS-CoV isolates and SARS-
73 related CoV (SARSr-CoV)[21,23,24], as well as with MERS-CoV[22]. Structural
74 characterization of two of these mAbs in complex with SARS-CoV S and MERS-CoV

75 S provided molecular-level information on the mechanisms of viral neutralization[14]. In
76 particular, while both mAbs blocked S^B attachment to the host receptor, the SARS-
77 CoV-neutralizing S230 mAb acted by functionally mimicking receptor-attachment and
78 promoting S fusogenic conformational rearrangements[14]. Another mechanism of
79 SARS-CoV neutralization was recently described for mAb CR3022, which bound a
80 cryptic epitope only accessible when at least two out of the three S^B domains of a S
81 trimer were in the open conformation[25,26]. However, none of these mAbs neutralize
82 SARS-CoV-2.
83
84 **Identification of a potent SARS-CoV-2 neutralizing mAb from a SARS survivor**
85 We previously identified a set of human neutralizing mAbs from an individual
86 infected with SARS-CoV in 2003 that potently inhibited both human and zoonotic
87 SARS-CoV isolates[21,23,27]. To characterize the potential cross-reactivity of these
88 antibodies with SARS-CoV-2, we performed a new memory B cell screening using
89 peripheral blood mononuclear cells collected in 2013 from the same patient. We
90 describe here nineteen mAbs from the initial screen (2004 blood draw)[21,23] and six
91 mAbs from the new screen (2013 blood draw). The identified mAbs had a broad V
92 gene usage and were not clonally related (**Table 1).** Eight out of the twenty five mAbs
93 bound to SARS-CoV-2 S and SARS-CoV S transfected CHO cells with EC_{50} values
94 ranging between 1.4 and 6,100 ng/ml, and 0.8 and 254 ng/ml, respectively **(Fig. 1a-**
95 **b)**. MAbs were further evaluated for binding to the SARS-CoV-2 and SARS-CoV S^B
96 domains as well as to the prefusion-stabilized OC43 S[28], MERS-CoV S[29,30], SARS-
97 CoV S[30] and SARS-CoV-2 S[6] ectodomain trimers. None of the mAbs studied bound to
98 prefusion OC43 S or MERS-CoV S ectodomain trimers, indicating a lack of cross-
99 reactivity outside the sarbecovirus subgenus **(Extended Data Fig.1)**. MAbs S303,
100 S304, S309 and S315 recognized the SARS-CoV-2 and SARS-CoV RBDs. In
101 particular, S309 bound with nanomolar affinity to both S^B domains, as determined by
102 biolayer interferometry **(Fig. 1c-d, Extended Data Fig. 2)**. Unexpectedly, S306 and
103 S310 stained cells expressing SARS-CoV-2 S at higher levels than those expressing
104 SARS-CoV S, yet it did not interact with SARS-CoV-2 or SARS-CoV S ectodomain
105 trimers and RBD constructs by ELISA. These results suggest that they may recognize
106 post-fusion SARS-CoV-2 S, which was recently proposed to be abundant on the
107 surface of authentic SARS-CoV-2 viruses[31] **(Fig. 1a-b and Extended Data Fig.3)**.

108 To evaluate the neutralization potency of the SARS-CoV-2 cross-reactive
109 mAbs, we carried out pseudovirus neutralization assays using a murine leukemia virus
110 (MLV) pseudotyping system[32]. S309 showed comparable neutralization potencies
111 against both SARS-CoV and SARS-CoV-2 pseudoviruses, whereas S303 neutralized
112 SARS-CoV-MLV but not SARS-CoV-2-MLV. S304 and S315 weakly neutralized
113 SARS-CoV-MLV and SARS-CoV-2-MLV (**Extended Data Fig.4**). In addition, S309
114 neutralized SARS-CoV-MLVs from isolates of the 3 phases of the 2002-2003 epidemic
115 with IC_{50} values comprised between 120 and 180 ng/ml and partially neutralized the
116 SARSr-CoV[33] WIV-1 (**Fig. 1e)**. Finally, mAb S309 potently neutralized authentic
117 SARS-CoV-2 (2019n-CoV/USA_WA1/2020) with an IC_{50} of 69 ng/ml (**Fig. 1f**).
118
119 **Structural basis of S309 cross-neutralization of SARS-CoV-2 and SARS-CoV**
120 To study the mechanisms of S309-mediated neutralization, we characterized
121 the complex between the S309 Fab fragment and a prefusion stabilized SARS-CoV-2
122 S ectodomain trimer[6] using single-particle cryoEM. Similar to our previous study of apo
123 SARS-CoV-2 S[6], 3D classification of the cryoEM data enabled identification of two
124 structural states: a trimer with one S^B domain open and a closed trimer. We determined
125 3D reconstructions of the SARS-CoV-2 S ectodomain trimer with a single open S^B
126 domain and in a closed state (applying 3-fold symmetry), both with three S309 Fabs
127 bound, at 3.7 Å and 3.3 Å resolution, respectively **(Fig. 2a-c, Extended Data Fig. 5**
128 **and Table 2)**. In parallel, we also determined a crystal structure of the S309 Fab at 3.3
129 Å resolution to assist model building (**Table 3**). The S309 Fab bound to the open S^B
130 domain is weakly resolved in the cryoEM map, due to marked conformational variability
131 of the upward pointing S^B domain, and was not modeled in density. The analysis below
132 is based on the closed state structure.
133 S309 recognizes a protein/glycan epitope on the SARS-CoV-2 S^B, distinct from
134 the receptor-binding motif. The epitope is accessible in both the open and closed S
135 states, explaining the stoichiometric binding of Fab to the S trimer **(Fig. 2a-c)**. The
136 S309 paratope is composed of all six CDR loops that burie a surface area of ~1,050$Å^2$
137 at the interface with S^B through electrostatic interactions and hydrophobic contacts.
138 The 20-residue long CDRH3 sits atop the S^B helix comprising residues 337-344 and
139 also contacts the edge of the S^B five-stranded β-sheet (residues 356-361), overall
140 accounting for ~50% of the buried surface area **(Fig. 2d-e)**. CDRL1 and CDRL2 extend
141 the epitope by interacting with the helix spanning residues 440-444 that is located near

142 the S 3-fold molecular axis. CDRH3 and CDRL2 sandwich the SARS-CoV-2 S glycan
143 at position N343 through contacts with the core fucose moiety (in agreement with the
144 detection of SARS-CoV-2 N343 core-fucosylated peptides by mass-spectrometry[34])
145 and to a lesser extent with the core N-acetyl-glucosamine (Fig. 2d). These latter
146 interactions bury an average surface of ~170 $Å^2$ and stabilize the N343 oligosaccharide
147 which is resolved to a much larger extent than in the apo SARS-CoV-2 S structures[6,9].
148 The structural data explain the S309 cross-reactivity between SARS-CoV-2 and
149 SARS-CoV as 19 out of 24 residues of the epitope are strictly conserved (**Fig. 2f** and
150 **Extended Data Fig. 6a-b)**. $R346_{SARS\text{-}CoV\text{-}2}$, $R357_{SARS\text{-}CoV\text{-}2}$, $N354_{SARS\text{-}CoV\text{-}2}$ and
151 $L441_{SARS\text{-}CoV\text{-}2}$ are conservatively substituted to $K333_{SARS\text{-}CoV}$, $K344_{SARS\text{-}CoV}$ (except for
152 SARS-CoV isolate GZ02 where it is $R444_{SARS\text{-}CoV}$), $E341_{SARS\text{-}CoV}$ and $I428_{SARS\text{-}CoV}$
153 whereas $K444_{SARS\text{-}CoV\text{-}2}$ is semi-conservatively substituted to $T431_{SARS\text{-}CoV}$, in
154 agreement with the comparable binding affinities to SARS-CoV and SARS-CoV-2 S
155 (**Fig. 1c).** The oligosaccharide at position N343 is also conserved in both viruses and
156 corresponds to SARS-CoV N330, for which we previously detected core-fucosylated
157 glycopeptides by mass spectrometry[14] which would allow for similar interactions with
158 the S309 Fab. Analysis of the S glycoprotein sequences of the 2,229 SARS-CoV-2
159 isolates reported to date indicates that several mutations have occurred with variable
160 frequency on the SARS-CoV-2 S ectodomain (**Extended Data Fig. 7a-b**) but no
161 mutations arose within the epitope recognized by S309 mAb. Finally, S309 contact
162 residues showed a high degree of conservation across clade 1, 2 and 3 sarbecovirus
163 human and animal isolates[35] (**Extended Data Fig. 7c).** Collectively, the structural data
164 indicate that S309 could neutralize all SARS-CoV-2 isolates circulating to date and
165 possibly most other zoonotic sarbecoviruses.
166
167 **Mechanism of S309-mediated neutralization of SARS-CoV-2 and SARS-CoV**
168 The cryoEM structure of S309 bound to SARS-CoV-2 S presented here
169 combined with the structures of SARS-CoV-2 S^B and SARS-CoV S^B in complex with
170 ACE2[16-18,36] indicate that the Fab engages an epitope distinct from the receptor-binding
171 motif and would not clash with ACE2 upon binding to S **(Figure 3a-b)**. Biolayer
172 interferometry analysis of S309 Fab or IgG binding to the SARS-CoV-2 S^B domain or
173 the S ectodomain trimer confirmed the absence of competition between the mAb and
174 ACE2 for binding to SARS-CoV-2 S **(Figure 3c and Extended Data Fig. 8)**.

175 To further investigate the mechanism of S309-mediated neutralization, we
176 compared side-by-side transduction of SARS-CoV-2-MLV in the presence of either
177 S309 Fab or S309 IgG. Both experiments yielded comparable IC_{50} values (3.8 and 3.5
178 nM, respectively), indicating similar potencies for IgG and Fab **(Fig. 3d)**. However, The
179 S309 IgG reached 100% neutralization, whereas the S309 Fab plateaued at ~80%
180 neutralization **(Fig. 3d)**. This result indicates that one or more IgG-specific bivalent
181 mechanisms, such as S trimer cross-linking, steric hindrance or aggregation of
182 virions[37], may contribute to the ability to fully neutralize pseudovirions.
183 Fc-dependent effector mechanisms, such as NK-mediated antibody-dependent
184 cell cytotoxicity (ADCC) and antibody-dependent cellular phagocytosis (ADCP) can
185 contribute to viral control in infected individuals. We observed efficient S309- and
186 S306-mediated ADCC of SARS-CoV-2 S-transfected cells, whereas the other mAbs
187 tested showed limited or no activity (**Fig. 3e and Extended Data Fig. 9a**). These
188 findings might be related to distinct binding orientations and/or positioning of the mAb
189 Fc fragment relative to the FcγRIIIa receptors. ADCC was observed only using NK
190 (effector) cells expressing the high-affinity FcγRIIIa variant (V158) but not the low-
191 affinity variant (F158) (**Fig. 3e**). These results, which we confirmed using a FcγRIIIa
192 cell reporter assay (**Fig. 3f**), suggest that S309 Fc engineering could potentially
193 enhance activation of NK cells with the low-affinity FcγRIIIa variant (F158)[38].
194 Macrophage or dendritic cell-mediated ADCP can contribute to viral control by clearing
195 virus and infected cells and by stimulating T cell response via presentation of viral
196 antigens[39,40]. Similar to the ADCC results, mAbs S309 and S306 showed the strongest
197 ADCP response **(Fig. 3g** and **Extended Data Fig. 8b)**. FcγRIIa signaling, however,
198 was only observed for S309 (**Fig. 3h**). These findings suggest that ADCP by
199 monocytes was dependent on both FcγRIIIa and FcγRIIa engagement. Collectively,
200 these results demonstrate that in addition to potent *in vitro* neutralization, S309 may
201 leverage additional protective mechanisms *in vivo*, as previously shown for other
202 antiviral antibodies[41,42].
203
204 **MAb cocktails enhance SARS-CoV-2 neutralization**
205 To gain more insight into the epitopes recognized by our panel of mAbs, we
206 used structural information, escape mutants analysis [23,27,30], and biolayer
207 inteferometry-based epitope binning to map the antigenic sites present on the SARS-

208 CoV and SARS-CoV-2 S^B domains (**Fig. 4a and Extended Data Fig.10)**. This analysis
209 identified at least four antigenic sites within the S^B domain of SARS-CoV targeted by
210 our panel of mAbs. The receptor-binding motif, which is targeted by S230, S227 and
211 S110, is termed site I. Sites II and III are defined by S315 and S124, respectively, and
212 the two sites were bridged by mAb S304. Site IV is defined by S309, S109, and S303
213 mAbs. Given the lower number of mAbs cross-reacting with SARS-CoV-2, we were
214 able to identify sites IV targeted by S309 and S303, and site II-III targeted by S304 and
215 S315 (**Fig. 4b**).
216 Based on the above findings, we evaluated the neutralization potency of the site
217 IV S309 mAb in combination with either the site II S315 mAb or site II-III S304 mAb.
218 Although S304 and S315 alone were weakly neutralizing, the combination of either of
219 these mAbs with S309 resulted in an enhanced neutralization potency, compared to
220 single mAbs, against both SARS-CoV-2-MLV and authentic SARS-CoV-2 **(Fig. 4c-d**
221 and **Fig. 1e)**. A synergistic effect between two non-competing anti-RBD mAbs has
222 been already reported for SARS-CoV[43] and our data extend this observation to SARS-
223 CoV-2, providing a proof-of-concept for the use of mAbs combinations to prevent or
224 control SARS-CoV-2.
225 In summary, our study identifies S309 as a human mAb with broad neutralizing
226 activity against multiple sarbecoviruses, including SARS-CoV-2, via recognition of a
227 highly conserved epitope in the S^B domain comprising the N343-glycan (N330 in
228 SARS-CoV S). Furthermore, S309 can recruit effector mechanisms and synergizes
229 with weakly neutralizing mAbs, which may mitigate the risk of viral escape. Our data
230 indicate the potential to discover potently neutralizing pan-sarbecovirus mAbs,
231 highlight antigenic sites to include in vaccine design, and pave the way to support
232 preparedness for future sarbecovirus outbreaks. As S309 bears the promise to be an
233 effective countermeasure to curtail the COVID-19 pandemic caused by SARS-CoV-2,
234 Fc variants of S309 with increased half-life and effector functions have entered an
235 accelerated development path towards clinical trials.
236
237
238

ACKNOWLEDGEMENTS

This study was supported by the National Institute of General Medical Sciences (R01GM120553, D.V.), the National Institute of Allergy and Infectious Diseases (HHSN272201700059C to DV and 75N93019C00062 to MSD)), a Pew Biomedical Scholars Award (D.V.), an Investigators in the Pathogenesis of Infectious Disease Award from the Burroughs Wellcome Fund (D.V.), the University of Washington Arnold and Mabel Beckman cryoEM center, the Pasteur Institute (M.A.T.) and the beamline 5.0.1 at the Advanced Light Source at Lawrence Berkley National Laboratory. We gratefully acknowledge the authors, originating and submitting laboratories of the sequences from GISAID's EpiFlu™ Database upon which this research is based.

AUTHOR CONTRIBUTIONS

A.C.W., K.F., M.S.D., D.V. and D.C. designed the experiments. A.C.W., M.A.T., S.J., E.C. expressed and purified the proteins. K.C., F.Z., S.J., E.C. sequenced and expressed antibodies. D.P., M.B., A.C.W. and S.B. performed binding assays. D.P., M.B., A.C.W., A.P., A.D.M. carried out pseudovirus neutralization assays. J.B.C., R.E.C. performed neutralization assays with authentic SARS-CoV-2. B.G. performed effector function assays. Y.J.P. prepared samples for cryoEM and collected the data. Y.J.P. and D.V. processed the data, built and refined the atomic models. A.C.W. crystallized the S309 Fab. Y.J.P. collected and processed the X-ray diffraction data and built and refined the atomic model. R.S., A.T. and G.S. performed bioinformatic and conservation analysis. A.L. provided key reagents. A.C.W., K.F., C.H.D., H.W.V., A.L., D.V., D.C. analyzed the data and prepared the manuscript with input from all authors.

DECLARATION OF INTERESTS

D.P., S.B., K.C., E.C., C.H-D., G.S., M.B., A.K., K.F., A.P. F.Z., S.J., B.G., A.D.M., A.L., A.T., H.W.V, R.S. and D.C. are employees of Vir Biotechnology Inc. and may hold shares in Vir Biotechnology Inc. M.S.D. is a consultant for Inbios, Eli Lilly, Vir Biotechnology, NGM Biopharmaceuticals, and Emergent BioSolutions and on the Scientific Advisory Board of Moderna. The Diamond laboratory at Washington

273 University School of Medicine has received sponsored research agreements from
274 Moderna. The other authors declare no competing financial interests.
275
276
277 **MATERIALS AND METHODS**
278
279 **Ethics statement**
280 Donors provided written informed consent for the use of blood and blood components
281 (such as sera), following approval by the Canton Ticino Ethics Committee, Switzerland.
282
283 **Antibody discovery and expression**
284 Monoclonal antibodies were isolated from EBV-immortalized memory B cells.
285 Recombinant antibodies were expressed in ExpiCHO cells transiently co-transfected
286 with plasmids expressing the heavy and light chain, as previously described[44]. Abs
287 S303, S304, S306, S309, S310 and S315 were expressed as rIgG-LS antibodies. The
288 LS mutation confers a longer half-life in vivo[45]. Antibodies S110 and S124 tested in
289 Fig. 1 and Extended Data Fig. 1 were purified mAbs produced from immortalized B
290 cells.
291
292 **Transient expression of recombinant SARS-CoV-2 protein and flow cytometry**
293 The full-length S gene of SARS-CoV-2 strain (SARS-CoV-2-S) isolate
294 BetaCoV/Wuhan-Hu-1/2019 (accession number MN908947) was codon optimized for
295 human cell expression and cloned into the phCMV1 expression vector (Genlantis).
296 Expi-CHO cells were transiently transfected with phCMV1-SARS-CoV-2-S, SARS-
297 spike_pcDNA.3 (strain SARS) or empty phCMV1 (Mock) using Expifectamine
298 CHO Enhancer. Two days after transfection, cells were collected for immunostaining
299 with mAbs. An Alexa647-labelled secondary antibody anti-human IgG Fc was used for
300 detection. Binding of mAbs to transfected cells was analyzed by flow-cytometry using a
301 ZE5 Cell Analyzer (Biorard) and FlowJo software (TreeStar). Positive binding was
302 defined by differential staining of CoV-S-transfectants versus mock-transfectants.
303
304 **Affinity determination and competition experiments using Octet (BLI, biolayer**
305 **interferometry)**

306 KD determination of full-length antibodies: Protein A biosensors (Pall ForteBio) were
307 used to immobilize recombinant antibodies at 2.7 μg/ml for 1min, after a hydration step
308 for 10 min with Kinetics Buffer (KB; 0.01% endotoxin-free BSA, 0.002% Tween-20,
309 0.005% NaN3 in PBS). Association curves were recorded for 5 minutes by incubating
310 the mAb-coated sensors with different concentration of SARS-CoV RBD (Sino
311 Biological) or SARS-CoV-2 RBD (produced in house; residues 331-550 of spike protein
312 from BetaCoV/Wuhan-Hu-1/2019, accession number MN908947). The highest RBD
313 concentration was 10 μg/ml, then serially diluted 1:2.5. Dissociation was recorded for
314 9 minutes by moving the sensors to wells containing KB. KD values were calculated
315 using a global fit model (Octet). Octet Red96 (ForteBio) equipment was used.
316 KD determination of full-length antibodies compared to Fab: His-tagged RBD of SARS-
317 CoV or SARS-CoV-2 were loaded at 3 µg/ml in KB for 15 minutes onto anti-HIS (HIS2)
318 biosensors (Molecular Devices, ForteBio). Association of mAb and Fab was performed
319 in KB at 15 μg/ml and 5 μg/ml respectively for 5 minutes. Dissociation in KB was
320 measured for 10 minutes.
321 MAbs competition experiments: His-tagged RBD of SARS-CoV or SARS-CoV-
322 2 was loaded for 5 minutes at 3 μg/ml in KB onto anti-Penta-HIS (HIS1K) biosensors
323 (Molecular Devices, ForteBio). Association of mAbs was performed in KB at 15 μg/ml.
324 ACE2 competition experiments: ACE2-His (Bio-Techne AG) was loaded for 30
325 minutes at 5 µg/ml in KB onto anti-HIS (HIS2) biosensors (Molecular Devices-
326 ForteBio).

327 SARS-CoV RBD-rabbitFc or SARS-CoV-2 RBD-mouseFc (Sino Biological Europe
328 GmbH) at 1 µg/ml was associated for 15 minutes, after a preincubation with or without
329 Ab (30 µg/ml, 30 minutes). Dissociation was monitored for 5 minutes.
330

331 **ELISA**

332 The following proteins were coated on 96 well ELISA plates at the following
333 concentrations: SARS-CoV RBD (Sino Biological, 40150-V08B1) at 1 µg/ml, SARS-
334 CoV-2 RBD (produced in house) at 10 µg/ml, ectodomains (stabilized prefusion trimer)
335 of SARS-CoV, SARS-CoV-2, OC43 and MERS, all at 1ug/ml. After blocking with 1%
336 BSA in PBS, antibodies es were added to the plates in a concentration range between
337 5 and 0.000028 μg/ml and incubated for 1 h at RT. Plates were washed and secondary
338 Ab Goat Anti Human IgG-AP (Southern Biotechnology: 2040-04) was added.

339 Substrate P-NitroPhenyl Phosphate (pNPP) (Sigma-Aldrich 71768) was used for
340 colour development. OD405 was read on an ELx808IU plate reader (Biotek).
341
342 **Measurement of Fc-effector functions**
343 ADCC assays were performed using ExpiCHO-S cells transient transfected with
344 SARS-CoV or SARS-CoV-2 S as targets. Target cells were incubated with titrated
345 concentrations of mAbs and after 10 minutes incubated with primary human NK cells
346 as effector cells at an effector:target ratio of 9:1. NK cells were isolated from fresh
347 blood of healthy donors using the MACSxpress NK Isolation Kit (Miltenyi Biotec, Cat.
348 Nr.: 130-098-185). ADCC was measured using LDH release assay (Cytotoxicity
349 Detection Kit (LDH) (Roche; Cat. Nr.: 11644793001) after 4 hours of incubation at
350 37°C.
351 ADCP assays were performed using ExpiCHO-S target cells transiently transfected
352 with SARS-CoV-2 S and fluorescently labeled with PKH67 Fluorescent Cell Linker Kits
353 (Sigma Aldrich, Cat. Nr.: MINI67) as targets. Target cells were incubated with titrated
354 concentrations of mAbs for 10minutes, followed by incubation with human PBMCs
355 isolated from healthy donors that were fluorescently labeled with Cell Trace Violet
356 (Invitrogen, Cat. Nr.: C34557) at an effector:target ratio of 20:1. After an overnight
357 incubation at 37°C, cells were stained with anti-human CD14-APC antibody (BD
358 Pharmingen, Cat. Nr.: 561708, Clone M5E2) to stain monocytes. Antibody-mediated
359 phagocytosis was determined by flow cytometry, gating on $CD14^+$ cells that were
360 double positive for cell trace violet and PKH67.
361 Determination of mAb-dependent activation of human FcγRIIIa or FcγRIIa was
362 performed using ExpiCHO cells transiently transfected with SARS-CoV-2 S
363 (BetaCoV/Wuhan-Hu-1/2019), incubated with titrated concentrations of mAbs for 10
364 minutes. ExpiCHO cells then were incubated with Jurkat cells expressing FcγRIIIa
365 receptor or FcγRIIa on their surface and stably transfected with NFAT-driven luciferase
366 gene (Promega, Cat. Nr.: G9798 and G7018) at an effector to target ratio of 6:1 for
367 FcγRIIIa and 5:1 for FcγRIIa. Activation of human FcγRs in this bioassay results in the
368 NFAT-mediated expression of the luciferase reporter gene. Luminescence was
369 measured after 21 hours of incubation at 37°C with 5% CO_2, using the Bio-Glo-TM
370 Luciferase Assay Reagent according to the manufacturer's instructions.
371

372 **Pseudovirus neutralization assays**

373 Murine leukemia virus (MLV)-based SARS-CoV S-pseudotyped viruses were prepared
374 as previously described[6,32]. HEK293T cells were co-transfected with a SARS-CoV,
375 SARS-CoV-2, CUHK, GZ02, or WiV1 S encoding-plasmid, an MLV Gag-Pol packaging
376 construct and the MLV transfer vector encoding aluciferase reporter using the
377 Lipofectamine 2000 transfection reagent (Life Technologies) according to the
378 manufacturer's instructions. Cells were incubated for 5 hours at 37°C with 8% CO_2 with
379 OPTIMEM transfection medium. DMEM containing 10% FBS was added for 72 hours.
380 VeroE6 cells or DBT cells transfected with human ACE2 were cultured in DMEM
381 containing 10% FBS, 1% PenStrep and plated into 96 well plates for 16-24 hours.
382 Concentrated pseudovirus with or without serial dilution of antibodies was incubated
383 for 1 hour and then added to the wells after washing 3X with DMEM. After 2-3 hours
384 DMEM containing 20% FBS and 2% PenStrep was added to the cells for 48 hours.
385 Following 48 hours of infection, One-Glo-EX (Promega) was added to the cells and
386 incubated in the dark for 5-10 minutes prior to reading on a Varioskan LUX plate reader
387 (ThermoFisher). Measurements were done in duplicate and relative luciferase units
388 (RLU) were converted to percent neutralization and plotted with a non-linear regression
389 curve fit in PRISM.

390

391 **Live virus neutralization assay**

392 SARS-CoV-2 strain 2019-nCoV/USA_WA1/2020 was obtained from the Centers for
393 Disease Control and Prevention (gift of Natalie Thornburg). Virus was passaged once
394 in Vero CCL81 cells (ATCC) and titrated by focus-forming assay on Vero E6 cells.
395 Serial dilutions of indicated mAbs were incubated with 10^2 focus forming units (FFU)
396 of SARS-CoV-2 for 1 hour at 37°C. MAb-virus complexes were added to Vero E6 cell
397 monolayers in 96-well plates and incubated at 37°C for 1 hour. Subsequently, cells
398 were overlaid with 1% (w/v) methylcellulose in MEM supplemented with 2% FBS.
399 Plates were harvested 30 hours later by removing overlays and fixed with 4% PFA in
400 PBS for 20 minutes at room temperature. Plates were washed and sequentially
401 incubated with 1 µg/mL of CR3022[46] anti-S antibody and HRP-conjugated goat anti-
402 human IgG in PBS supplemented with 0.1% saponin and 0.1% BSA. SARS-CoV-2-
403 infected cell foci were visualized using TrueBlue peroxidase substrate (KPL) and

404 quantitated on an ImmunoSpot microanalyzer (Cellular Technologies). Data were
405 processed using Prism software (GraphPad Prism 8.0).
406
407 **Recombinant Spike ectodomain production**
408 The SARS-CoV-2 2P S (Genbank: YP_009724390.1) ectodomain was produced in
409 500mL cultures of HEK293F cells grown in suspension using FreeStyle 293 expression
410 medium (Life technologies) at 37°C in a humidified 8% CO2 incubator rotating at 130
411 r.p.m, as previously reported[6]. The culture was transfected using 293fectin
412 (ThermoFisher Scientific) with cells grown to a density of 10^6 cells per mL and
413 cultivated for three days. The supernatant was harvested and cells were resuspended
414 for another three days, yielding two harvests. Clarified supernatants were purified
415 using a 5mL Cobalt affinity column (Takara). Purified protein was filtered or
416 concentrated and flash frozen in a buffer containing 50 mM Tris pH 8.0 and 150 mM
417 NaCl prior to cryoEM analysis. The SARS-CoV S, HCoV-OC43 S and MERS-CoV S
418 constructs were previously described[14,28] and produced similarly to SARS-CoV-2 2P
419 S.
420
421 **CryoEM sample preparation and data collection**.
422 3 µL of SARS-CoV-2 S at 1.6 mg/mL was mixed with 0.45 µL of S309 Fab at 7.4 mg/mL
423 for 1 min at room temperature before application onto a freshly glow discharged 1.2/1.3
424 UltraFoil grid (300 mesh). Plunge freezing used a vitrobot MarkIV (ThermoFisher
425 Scientific) using a blot force of 0 and 6.5 second blot time at 100% humidity and 25°C.
426 Data were acquired using the Leginon software [47] to control an FEI Titan Krios
427 transmission electron microscope operated at 300 kV and equipped with a Gatan K2
428 Summit direct detector and Gatan Quantum GIF energy filter, operated in zero-loss
429 mode with a slit width of 20 eV. Automated data collection was carried out using
430 Leginon at a nominal magnification of 130,000x with a pixel size of 0.525 Å with tilt
431 angles ranging between 20˚ and 50˚, as previously described[48]. The dose rate was
432 adjusted to 8 counts/pixel/s, and each movie was acquired in super-resolution mode
433 fractionated in 50 frames of 200 ms. 3,900 micrographs were collected in a single
434 session with a defocus range comprised between 1.0 and 3.0 µm.
435
436
437

438 **CryoEM data processing**

439 Movie frame alignment, estimation of the microscope contrast-transfer function
440 parameters, particle picking and extraction were carried out using Warp [49]. Particle
441 images were extracted with a box size of 800 binned to 400 yielding a pixel size of 1.05
442 Å. For each data set two rounds of reference-free 2D classification were performed
443 using cryoSPARC [50] to select well-defined particle images. Subsequently, two rounds
444 of 3D classification with 50 iterations each (angular sampling 7.5˚ for 25 iterations and
445 1.8˚ with local search for 25 iterations), using our previously reported closed SARS-
446 CoV-2 S structure[6] as initial model, were carried out using Relion [51] without imposing
447 symmetry to separate distinct SARS-CoV-2 S conformations. 3D refinements were
448 carried out using non-uniform refinement along with per-particle defocus refinement in
449 cryoSPARC[50]. Particle images were subjected to Bayesian polishing [52] before
450 performing another round of non-uniform refinement in cryoSPARC [50] followed by per-
451 particle defocus refinement and again non-uniform refinement. Reported resolutions
452 are based on the gold-standard Fourier shell correlation (FSC) of 0.143 criterion and
453 Fourier shell correlation curves were corrected for the effects of soft masking by high-
454 resolution noise substitution[53].

455

456 **CryoEM model building and analysis**.

457 UCSF Chimera [54] and Coot were used to fit atomic models (PDB 6VXX and PDB
458 6VYB) into the cryoEM maps. The Fab was subsequently manually built using
459 Coot[55,56]. N-linked glycans were hand-built into the density where visible and the
460 models were refined and relaxed using Rosetta[57]. Glycan refinement relied on a
461 dedicated Rosetta protocol, which uses physically realistic geometries based on prior
462 knowledge of saccharide chemical properties [58], and was aided by using both
463 sharpened and unsharpened maps. Models were analyzed using MolProbity [59],
464 EMringer [60], Phenix [61] and privateer [62] to validate the stereochemistry of both the
465 protein and glycan components. Figures were generated using UCSF ChimeraX [63].

466

467 **Crystallization and X-ray structure determination of Fab S309**

468 Fab S309 crystals were grown in hanging drop set up with a mosquito at 20°C using
469 150 nL protein solution in Tris HCl pH 8.0, 150 mM NaCl and 150nL mother liquor
470 solution containing 1.1 M Sodium Malonate, 0.1 M HEPES, pH 7.0 and 0.5% (w/v)
471 Jeffamine ED-2001. Crystals were cryo-protected using the mother liquor solution

472 supplemented with 30% glycerol. The dataset was collected at ALS beamline 5.0.2
473 and processed to 3.3 Å resolution in space group $P4_12_12$ using mosflm[64] and
474 Aimless[65]. The structure of Fab S309 was solved by molecular replacement using
475 Phaser[66] and homology models as search models. The coordinates were improved
476 and completed using Coot[55] and refined with REFMAC5[67]. Crystallographic data
477 collection and refinement statistics are shown in Table 3.
478
479 **Sequence alignment**
480 SARS-CoV-2 genomics sequences were downloaded from GISAID on March
481 29th 2020, using the "complete (>29,000 bp)" and "low coverage exclusion" filters. Bat
482 and pangolin sequences were removed to yield human-only sequences. The spike
483 ORF was localized by performing reference protein (YP_009724390.1)-genome
484 alignments with GeneWise2. Incomplete matches and indel-containing ORFs were
485 rescued and included in downstream analysis. Nucleotide sequences were
486 translated *in silico* using seqkit. Sequences with more than 10% undetermined
487 aminoacids (due to N basecalls) were removed. Multiple sequence alignment was
488 performed using MAFFT. Variants were determined by comparison of aligned
489 sequences (n=2,229) to the reference sequence using the R/Bioconductor package
490 Biostrings. A similar strategy was used to extract and translate spike protein
491 sequences from SARS-CoV genomes sourced from ViPR (search criteria: SARS-
492 related coronavirus, full-length genomes, human host, deposited before December
493 2019 to exclude SARS-CoV-2, n=53). Sourced SARS-CoV genome sequences
494 comprised all the major published strains, such as Urbani, Tor2, TW1, P2, Frankfurt1,
495 among others. Pangolin sequences as shown by Tsan-Yuk Lam et al[68] were sourced
496 from GISAID. Bat sequences from the three clades of sarbecoviruses as shown by Lu
497 et al[35] were sourced from Genbank. Civet and racoon dog sequences were similarly
498 sourced from Genbank.
499
500

References

1 Zhou, P. *et al.* A pneumonia outbreak associated with a new coronavirus of probable bat origin. *Nature*, doi:10.1038/s41586-020-2012-7 (2020).

2 Zhu, N. *et al.* A Novel Coronavirus from Patients with Pneumonia in China, 2019. *N Engl J Med*, doi:10.1056/NEJMoa2001017 (2020).

3 Tortorici, M. A. & Veesler, D. Structural insights into coronavirus entry. *Adv Virus Res* **105**, 93-116, doi:10.1016/bs.aivir.2019.08.002 (2019).

4 Walls, A. C. *et al.* Cryo-electron microscopy structure of a coronavirus spike glycoprotein trimer. *Nature* **531**, 114-117, doi:10.1038/nature16988 10.1038/nature16988. Epub 2016 Feb 8. (2016).

5 Walls, A. C. *et al.* Tectonic conformational changes of a coronavirus spike glycoprotein promote membrane fusion. *Proceedings of the National Academy of Sciences* **114**, 11157-11162, doi:10.1073/pnas.1708727114 (2017).

6 Walls, A. C. *et al.* Structure, function and antigenicity of the SARS-CoV-2 spike glycoprotein. *bioRxiv*, 2020.2002.2019.956581, doi:10.1101/2020.02.19.956581 (2020).

7 Hoffmann, M. *et al.* SARS-CoV-2 Cell Entry Depends on ACE2 and TMPRSS2 and Is Blocked by a Clinically Proven Protease Inhibitor. *Cell*, doi:10.1016/j.cell.2020.02.052 (2020).

8 Letko, M., Marzi, A. & Munster, V. Functional assessment of cell entry and receptor usage for SARS-CoV-2 and other lineage B betacoronaviruses. *Nature Microbiology*, doi:10.1038/s41564-020-0688-y (2020).

9 Wrapp, D. *et al.* Cryo-EM structure of the 2019-nCoV spike in the prefusion conformation. *Science*, doi:10.1126/science.abb2507 (2020).

10 Li, W. *et al.* Receptor and viral determinants of SARS-coronavirus adaptation to human ACE2. *EMBO J* **24**, 1634-1643, doi:10.1038/sj.emboj.7600640 10.1038/sj.emboj.7600640. Epub 2005 Mar 24. (2005).

11 Rossen, J. W. *et al.* The viral spike protein is not involved in the polarized sorting of coronaviruses in epithelial cells. *J Virol* **72**, 497-503 (1998).

12 Walls, A. C. *et al.* Glycan shield and epitope masking of a coronavirus spike protein observed by cryo-electron microscopy. *Nat Struct Mol Biol* **23**, 899-905, doi:10.1038/nsmb.3293 10.1038/nsmb.3293. Epub 2016 Sep 12. (2016).

13 Xiong, X. *et al.* Glycan shield and fusion activation of a deltacoronavirus spike glycoprotein fine-tuned for enteric infections. *J Virol*, doi:10.1128/JVI.01628-17 10.1128/JVI.01628-17. (2017).

14 Walls, A. C. *et al.* Unexpected Receptor Functional Mimicry Elucidates Activation of Coronavirus Fusion. *Cell* **176**, 1026-1039 e1015, doi:10.1016/j.cell.2018.12.028 10.1016/j.cell.2018.12.028. Epub 2019 Jan 31. (2019).

15 Yang, Y. *et al.* Two Mutations Were Critical for Bat-to-Human Transmission of Middle East Respiratory Syndrome Coronavirus. *J Virol* **89**, 9119-9123, doi:10.1128/JVI.01279-15 10.1128/JVI.01279-15. Epub 2015 Jun 10. (2015).

16 Yan, R. *et al.* Structural basis for the recognition of SARS-CoV-2 by full-length human ACE2. *Science* **367**, 1444-1448, doi:10.1126/science.abb2762 (2020).

17 Shang, J. *et al.* Structural basis of receptor recognition by SARS-CoV-2. *Nature*, doi:10.1038/s41586-020-2179-y (2020).

18 Lan, J. *et al.* Structure of the SARS-CoV-2 spike receptor-binding domain bound to the ACE2 receptor. *Nature*, doi:10.1038/s41586-020-2180-5 (2020).
19 Corti, D. *et al.* Protective monotherapy against lethal Ebola virus infection by a potently neutralizing antibody. *Science* **351**, 1339-1342, doi:10.1126/science.aad5224 (2016).
20 Levine, M. M. Monoclonal Antibody Therapy for Ebola Virus Disease. *N Engl J Med* **381**, 2365-2366, doi:10.1056/NEJMe1915350 (2019).
21 Traggiai, E. *et al.* An efficient method to make human monoclonal antibodies from memory B cells: potent neutralization of SARS coronavirus. *Nat Med* **10**, 871-875, doi:10.1038/nm1080
10.1038/nm1080. Epub 2004 Jul 11. (2004).
22 Corti, D. *et al.* Prophylactic and postexposure efficacy of a potent human monoclonal antibody against MERS coronavirus. *Proc Natl Acad Sci U S A* **112**, 10473-10478, doi:10.1073/pnas.1510199112
10.1073/pnas.1510199112. Epub 2015 Jul 27. (2015).
23 Rockx, B. *et al.* Structural basis for potent cross-neutralizing human monoclonal antibody protection against lethal human and zoonotic severe acute respiratory syndrome coronavirus challenge. *J Virol* **82**, 3220-3235, doi:10.1128/JVI.02377-07
10.1128/JVI.02377-07. Epub 2008 Jan 16. (2008).
24 Menachery, V. D. *et al.* SARS-like WIV1-CoV poised for human emergence. *Proc Natl Acad Sci U S A* **113**, 3048-3053, doi:10.1073/pnas.1517719113
10.1073/pnas.1517719113. Epub 2016 Mar 14. (2016).
25 Yuan, M. *et al.* A highly conserved cryptic epitope in the receptor-binding domains of SARS-CoV-2 and SARS-CoV. *Science*, doi:10.1126/science.abb7269 (2020).
26 Joyce, M. G. *et al.* A Cryptic Site of Vulnerability on the Receptor Binding Domain of the SARS-CoV-2 Spike Glycoprotein. *bioRxiv*, 2020.2003.2015.992883, doi:10.1101/2020.03.15.992883 (2020).
27 Rockx, B. *et al.* Escape from human monoclonal antibody neutralization affects in vitro and in vivo fitness of severe acute respiratory syndrome coronavirus. *J Infect Dis* **201**, 946-955, doi:10.1086/651022
10.1086/651022. (2010).
28 Tortorici, M. A. *et al.* Structural basis for human coronavirus attachment to sialic acid receptors. *Nat Struct Mol Biol* **26**, 481-489, doi:10.1038/s41594-019-0233-y (2019).
29 Park, Y. J. *et al.* Structures of MERS-CoV spike glycoprotein in complex with sialoside attachment receptors. *Nat Struct Mol Biol* **26**, 1151-1157, doi:10.1038/s41594-019-0334-7 (2019).
30 Walls, A. C. *et al.* Unexpected Receptor Functional Mimicry Elucidates Activation of Coronavirus Fusion. *Cell* **176**, 1026-1039.e1015, doi:10.1016/j.cell.2018.12.028 (2019).
31 Liu, C. *et al.* Viral Architecture of SARS-CoV-2 with Post-Fusion Spike Revealed by Cryo-EM. *bioRxiv*, 2020.2003.2002.972927, doi:10.1101/2020.03.02.972927 (2020).
32 Millet, J. K. & Whittaker, G. R. Murine Leukemia Virus (MLV)-based Coronavirus Spike-pseudotyped Particle Production and Infection. *Bio Protoc* **6**, doi:10.21769/BioProtoc.2035
10.21769/BioProtoc.2035. (2016).

599 33 Ge, X. Y. *et al.* Isolation and characterization of a bat SARS-like coronavirus
600 that uses the ACE2 receptor. *Nature* **503**, 535-538, doi:10.1038/nature12711
601 10.1038/nature12711. Epub 2013 Oct 30. (2013).
602 34 Watanabe, Y., Allen, J. D., Wrapp, D., McLellan, J. S. & Crispin, M. Site-specific
603 analysis of the SARS-CoV-2 glycan shield. *bioRxiv*, 2020.2003.2026.010322,
604 doi:10.1101/2020.03.26.010322 (2020).
605 35 Lu, R. *et al.* Genomic characterisation and epidemiology of 2019 novel
606 coronavirus: implications for virus origins and receptor binding. *Lancet* **395**,
607 565-574, doi:10.1016/S0140-6736(20)30251-8 (2020).
608 36 Li, F., Li, W., Farzan, M. & Harrison, S. C. Structure of SARS coronavirus spike
609 receptor-binding domain complexed with receptor. *Science* **309**, 1864-1868,
610 doi:10.1126/science.1116480 (2005).
611 37 Klasse, P. J. & Sattentau, Q. J. Occupancy and mechanism in antibody-
612 mediated neutralization of animal viruses. *J Gen Virol* **83**, 2091-2108,
613 doi:10.1099/0022-1317-83-9-2091 (2002).
614 38 Wang, X., Mathieu, M. & Brezski, R. J. IgG Fc engineering to modulate antibody
615 effector functions. *Protein Cell* **9**, 63-73, doi:10.1007/s13238-017-0473-8
616 (2018).
617 39 He, W. *et al.* Alveolar macrophages are critical for broadly-reactive antibody-
618 mediated protection against influenza A virus in mice. *Nat Commun* **8**, 846,
619 doi:10.1038/s41467-017-00928-3 (2017).
620 40 DiLillo, D. J. & Ravetch, J. V. Differential Fc-Receptor Engagement Drives an
621 Anti-tumor Vaccinal Effect. *Cell* **161**, 1035-1045, doi:10.1016/j.cell.2015.04.016
622 (2015).
623 41 Corti, D. *et al.* A neutralizing antibody selected from plasma cells that binds to
624 group 1 and group 2 influenza A hemagglutinins. *Science* **333**, 850-856,
625 doi:10.1126/science.1205669 (2011).
626 42 Hessell, A. J. *et al.* Fc receptor but not complement binding is important in
627 antibody protection against HIV. *Nature* **449**, 101-104,
628 doi:10.1038/nature06106 (2007).
629 43 ter Meulen, J. *et al.* Human monoclonal antibody combination against SARS
630 coronavirus: synergy and coverage of escape mutants. *PLoS Med* **3**, e237,
631 doi:10.1371/journal.pmed.0030237 (2006).
632 44 Stettler, K. *et al.* Specificity, cross-reactivity, and function of antibodies elicited
633 by Zika virus infection. *Science* **353**, 823-826, doi:10.1126/science.aaf8505
634 (2016).
635 45 Zalevsky, J. *et al.* Enhanced antibody half-life improves in vivo activity. *Nat*
636 *Biotechnol* **28**, 157-159, doi:10.1038/nbt.1601 (2010).
637 46 Tian, X. *et al.* Potent binding of 2019 novel coronavirus spike protein by a SARS
638 coronavirus-specific human monoclonal antibody. *Emerg Microbes Infect* **9**,
639 382-385, doi:10.1080/22221751.2020.1729069 (2020).
640 47 Suloway, C. *et al.* Automated molecular microscopy: the new Leginon system.
641 *Journal of structural biology* **151**, 41-60, doi:10.1016/j.jsb.2005.03.010 (2005).
642 48 Tan, Y. Z. *et al.* Addressing preferred specimen orientation in single-particle
643 cryo-EM through tilting. *Nat Methods* **14**, 793-796, doi:10.1038/nmeth.4347
644 (2017).
645 49 Tegunov, D. & Cramer, P. Real-time cryo-electron microscopy data
646 preprocessing with Warp. *Nature methods*, doi:10.1038/s41592-019-0580-y
647 (2019).

50 Punjani, A., Rubinstein, J. L., Fleet, D. J. & Brubaker, M. A. cryoSPARC: algorithms for rapid unsupervised cryo-EM structure determination. *Nature methods* **14**, 290-296, doi:10.1038/nmeth.4169 (2017).
51 Zivanov, J. *et al.* New tools for automated high-resolution cryo-EM structure determination in RELION-3. *Elife* **7**, doi:10.7554/eLife.42166 10.7554/eLife.42166. (2018).
52 Zivanov, J., Nakane, T. & Scheres, S. H. W. A Bayesian approach to beam-induced motion correction in cryo-EM single-particle analysis. *IUCrJ* **6**, doi:doi:10.1107/S205225251801463X (2019).
53 Scheres, S. H. & Chen, S. Prevention of overfitting in cryo-EM structure determination. *Nature methods* **9**, 853-854, doi:10.1038/nmeth.2115 (2012).
54 Goddard, T. D., Huang, C. C. & Ferrin, T. E. Visualizing density maps with UCSF Chimera. *Journal of structural biology* **157**, 281-287, doi:10.1016/j.jsb.2006.06.010 (2007).
55 Emsley, P., Lohkamp, B., Scott, W. G. & Cowtan, K. Features and development of Coot. *Acta Crystallogr D Biol Crystallogr* **66**, 486-501, doi:10.1107/S0907444910007493 (2010).
56 Brown, A. *et al.* Tools for macromolecular model building and refinement into electron cryo-microscopy reconstructions. *Acta Crystallogr D Biol Crystallogr* **71**, 136-153, doi:10.1107/S1399004714021683 (2015).
57 Wang, R. Y. *et al.* Automated structure refinement of macromolecular assemblies from cryo-EM maps using Rosetta. *eLife* **5**, doi:10.7554/eLife.17219 (2016).
58 Frenz, B. D. R., S.; Borst A.J.; Walls, A.C.; Adolf-Bryfogle, J.; Schief, W.R.; Veesler, D.; DiMaio, F. Automatically fixing errors in glycoprotein structures with Rosetta. *Structure* **27**, 1-6, doi:https://doi.org/10.1016/j.str.2018.09.006 (2019).
59 Chen, V. B. *et al.* MolProbity: all-atom structure validation for macromolecular crystallography. *Acta Crystallogr D Biol Crystallogr* **66**, 12-21, doi:10.1107/S0907444909042073 (2010).
60 Barad, B. A. *et al.* EMRinger: side chain-directed model and map validation for 3D cryo-electron microscopy. *Nat Methods* **12**, 943-946, doi:10.1038/nmeth.3541 10.1038/nmeth.3541. Epub 2015 Aug 17. (2015).
61 Liebschner, D. *et al.* Macromolecular structure determination using X-rays, neutrons and electrons: recent developments in Phenix. *Acta Crystallogr D Struct Biol* **75**, 861-877, doi:10.1107/S2059798319011471 (2019).
62 Agirre, J. *et al.* Privateer: software for the conformational validation of carbohydrate structures. *Nature structural & molecular biology* **22**, 833-834, doi:10.1038/nsmb.3115 (2015).
63 Goddard, T. D. *et al.* UCSF ChimeraX: Meeting modern challenges in visualization and analysis. *Protein Sci* **27**, 14-25, doi:10.1002/pro.3235 (2018).
64 Battye, T. G., Kontogiannis, L., Johnson, O., Powell, H. R. & Leslie, A. G. iMOSFLM: a new graphical interface for diffraction-image processing with MOSFLM. *Acta Crystallogr D Biol Crystallogr* **67**, 271-281, doi:10.1107/S0907444910048675 (2011).
65 Evans, P. R. & Murshudov, G. N. How good are my data and what is the resolution? *Acta Crystallogr D Biol Crystallogr* **69**, 1204-1214, doi:10.1107/S0907444913000061 (2013).
66 McCoy, A. J. *et al.* Phaser crystallographic software. *J Appl Crystallogr* **40**, 658-674, doi:10.1107/S0021889807021206 (2007).

67 Murshudov, G. N. *et al.* REFMAC5 for the refinement of macromolecular crystal structures. *Acta Crystallogr D Biol Crystallogr* **67**, 355-367, doi:10.1107/S0907444911001314 (2011).
68 Lam, T. T. *et al.* Identifying SARS-CoV-2 related coronaviruses in Malayan pangolins. *Nature*, doi:10.1038/s41586-020-2169-0 (2020).

Figure 1

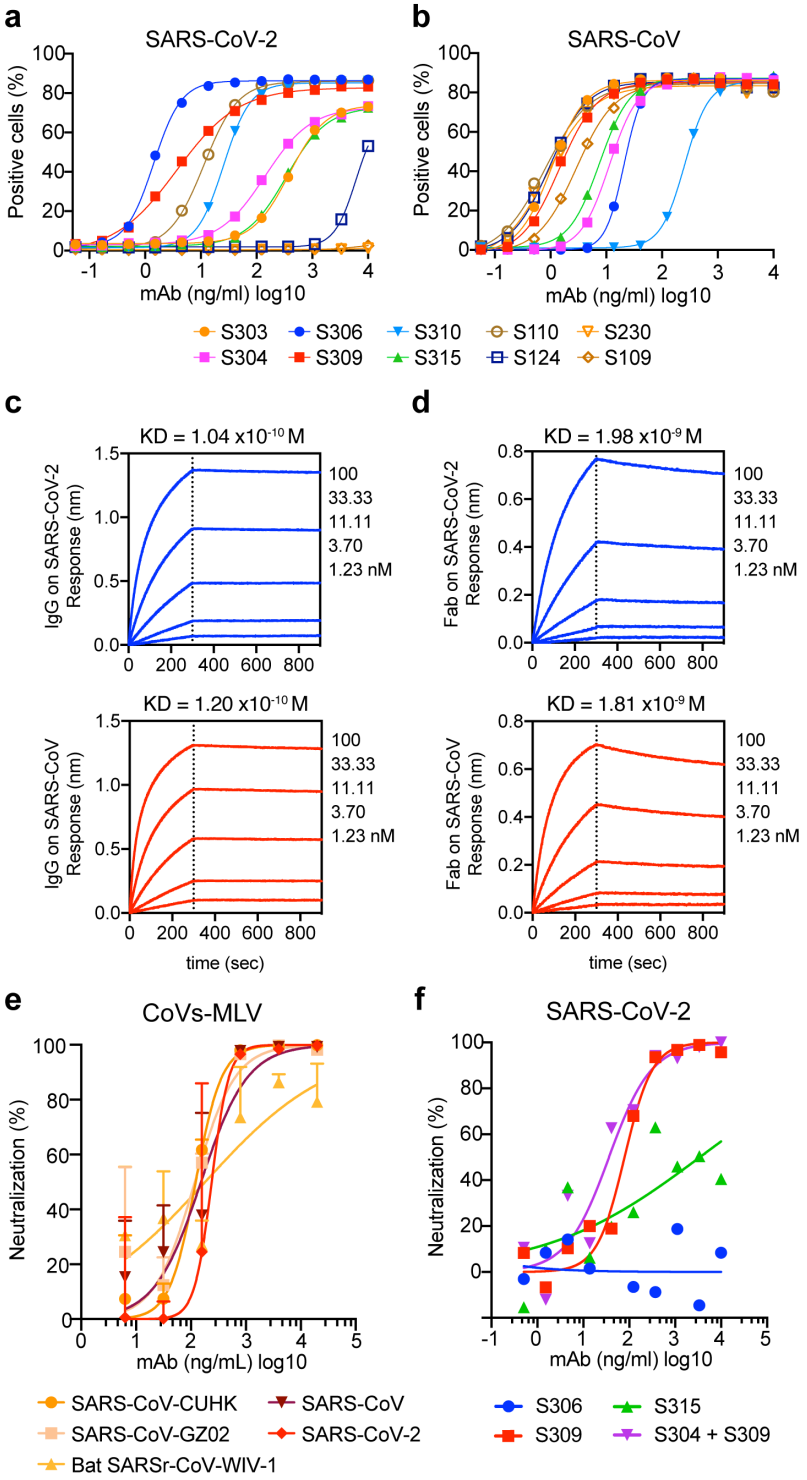

Figure 1: Identification of a potent SARS-CoV-2 neutralizing mAb from a SARS survivor. a-b, Binding of a panel of mAbs isolated from a SARS-immune patient to the SARS-CoV-2 (**a**) or SARS-CoV (**b**) S glycoproteins expressed at the surface of ExpiCHO cells (symbols are means of duplicates from one experiment). **c-d**, Affinity measurement of S309 full-length IgG1 and Fab for SARS-CoV-2 and SARS-CoV S^B domains measured using biolayer interferometry. **e**, Neutralization of SARS-CoV-2-MLV, SARS-CoV-MLV (bearing S from various isolates) and other sarbecovirus isolates by mAb S309. **f**, Neutralization of authentic SARS-CoV-2 (strain n-CoV/USA_WA1/2020) by mAbs as measured by a focus-forming assay on Vero E6 cells. (**e-f**) mean±SD (**e**) or means (**f**) of duplicates are shown. One representative out of two experiments is shown.

Figure 2

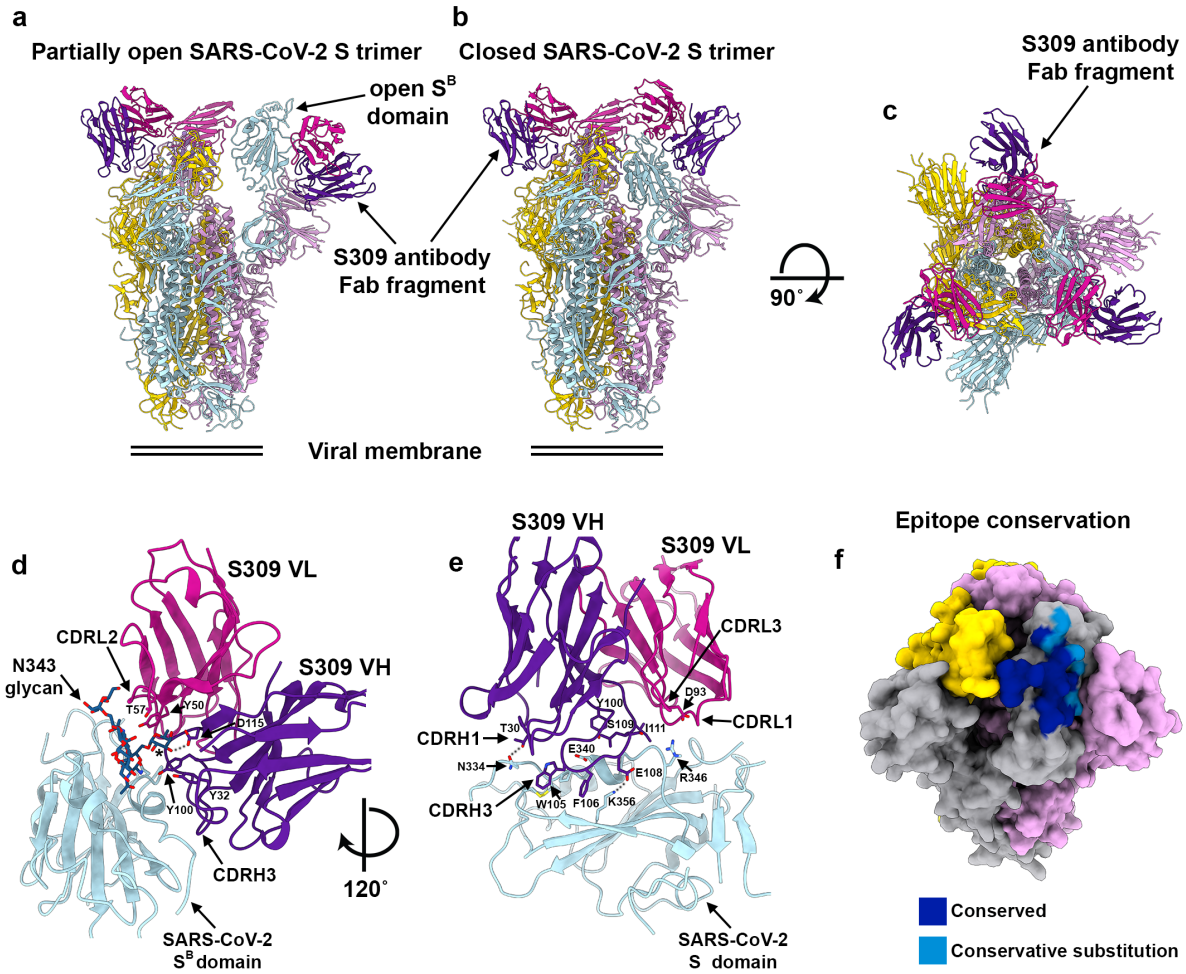

Figure 2: CryoEM structures of the SARS-CoV-2 S glycoprotein in complex with the S309 neutralizing antibody Fab fragment. a, Ribbon diagram of the partially open SARS-CoV-2 S trimer (one S^B domain is open) bound to three S309 Fabs. **b-c,** Ribbon diagrams of the closed SARS-CoV-2 S trimer bound to three S309 Fabs shown in two orthogonal orientations. **d,** Close-up view of the S309 epitope showing the contacts formed with the core fucose (labeled with a star) and the core N-acetyl-glucosamine of the oligosaccharide at position N343. **e,** Close-up view of the S309 epitope showing the 20-residue long CDRH3 siting atop the S^B helix comprising residues 337-344. The oligosaccharide at position N343 is omitted for clarity. In panels (**c-d**), selected residues involved in interactions between S309 and SARS-CoV-2 S are shown. **F,** Molecular surface representation of the SARS-CoV-2 S trimer showing the S309 footprint colored by residue conservation on one protomer among SARS-CoV-2 and SARS-CoV S glycoproteins. The other two protomers are colored pink and gold.

Figure 3

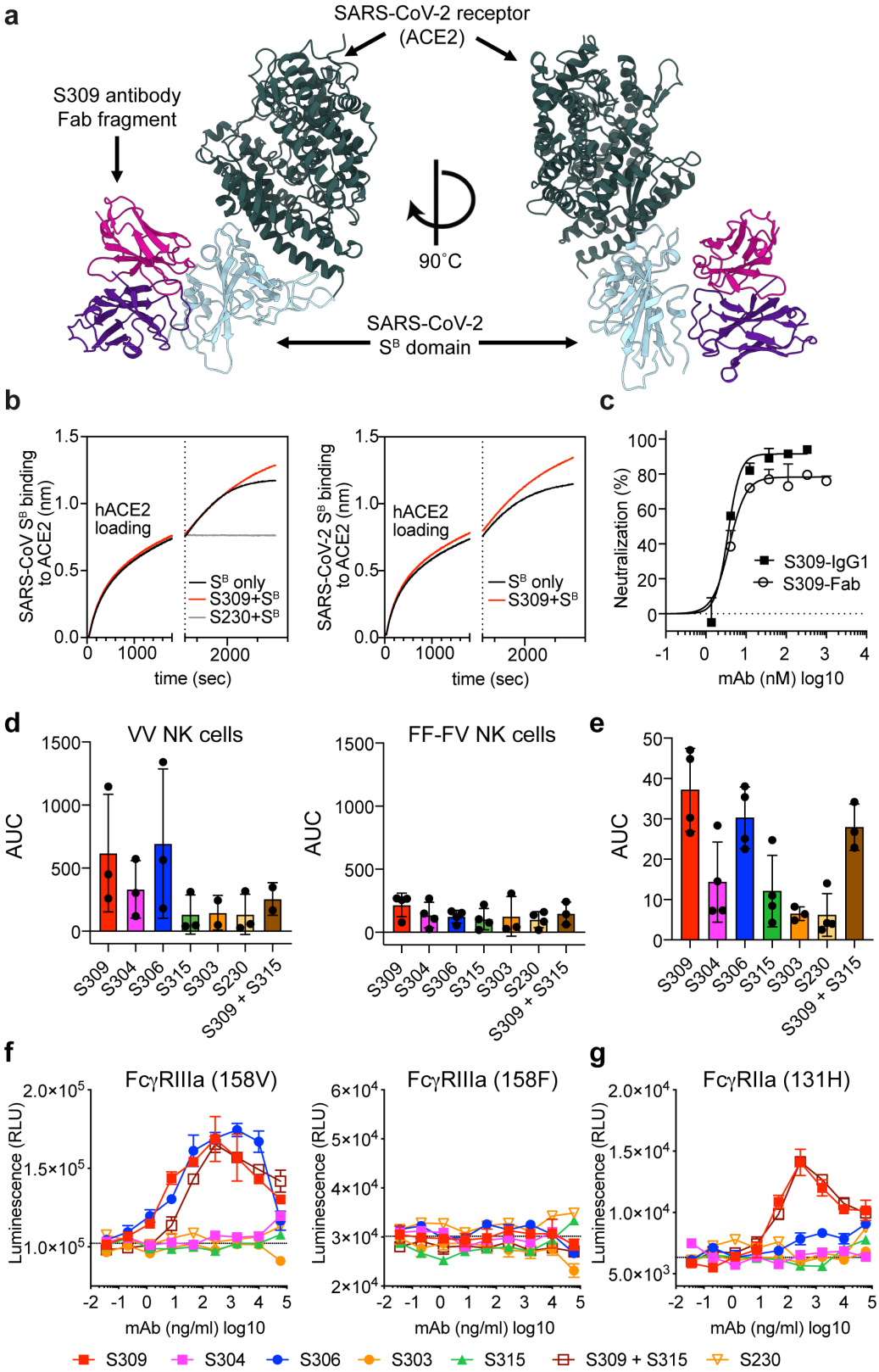

Figure 3: Mechanism of neutralization of S309 mAb. See next page for caption

Figure 3: Mechanism of neutralization of S309 mAb. **a-b**, Ribbon diagrams of S309 and ACE2 bound to SARS-CoV-2 S^B. This composite model was generated using the SARS-CoV-2 S/S309 cryoEM structure reported here and a crystal structure of SARS-CoV-2 S bound to ACE2[16]. **c**, Competition of S309 or S230 mAbs with ACE2 to bind to SARS-CoV S^B (left panel) and SARS-CoV-2 S^B (right panel). ACE2 was immobilized at the surface of biosensors before incubation with S^B domain alone or S^B precomplexed with mAbs. The vertical dashed line indicates the start of the association of mAb-complexed or free S^B to solid-phase ACE2. **d,** Neutralization of SARS-CoV-MLV by S309 IgG1 or S309 Fab, plotted in nM (means ±SD is shown, one out of two experiments is shown). **e,** mAb-mediated ADCC using primary NK effector cells and SARS-CoV-2 S-expressing ExpiCHO as target cells. Bar graph shows the average area under the curve (AUC) for the responses of 3-4 donors genotyped for their FcγRIIIa (mean±SD, from two independent experiments). **f,** Activation of high affinity (V158) or low affinity (F158) FcγRIIIa was measured using Jurkat reporter cells and SARS-CoV-2 S-expressing ExpiCHO as target cells (one experiment, one or two measurements per mAb). **g,** mAb-mediated ADCP using Cell Trace Violet-labelled PBMCs as phagocytic cells and PKF67-labelled SARS-CoV-2 S-expressing ExpiCHO as target cells. Bar graph shows the average area under the curve (AUC) for the responses of four donor (mean±SD, from two independent experiments). **h,** Activation of FcγRIIa measured using Jurkat reporter cells and SARS-CoV-2 S-expressing ExpiCHO as target cells (one experiment, one or two measurements per mAb).

Figure 4

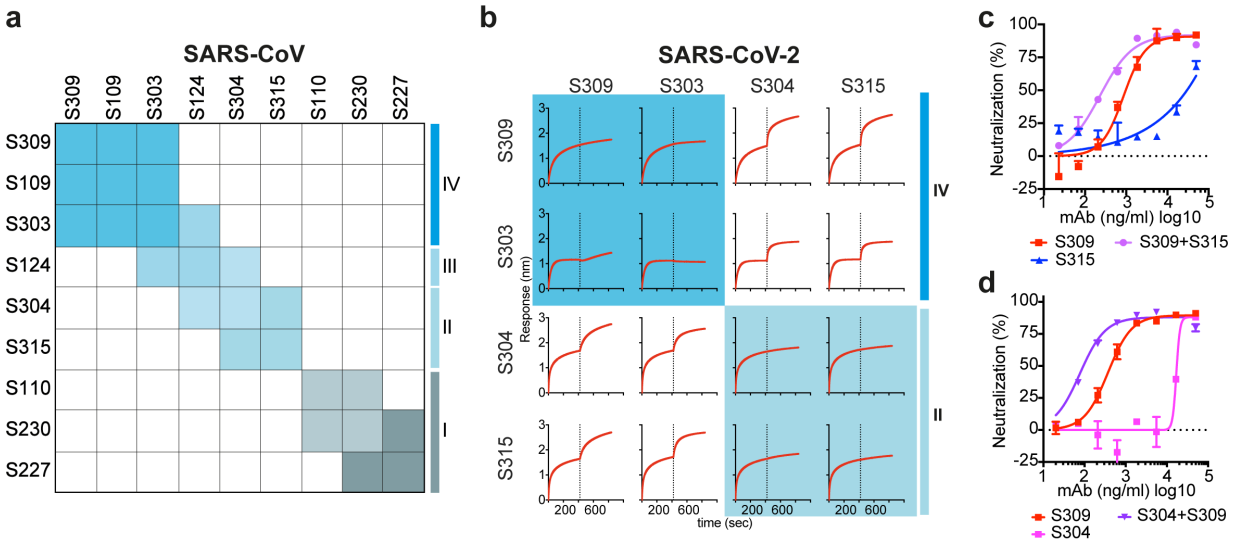

Figure 4: MAb cocktails enhance SARS-CoV-2 neutralization. a, Heat map showing the competition of mAb pairs for binding to the SARS-CoV S^B domain as measured by biolayer interferometry (as shown in Extended Data Fig. 9). **b,** Competition of mAb pairs for binding to the SARS-CoV-2 S^B domain **. c-d,** Neutralization of SARS-CoV-2-MLV by S309 combined with an equimolar amount of S304 or S315 mAbs. For mAb cocktails the concentration on the x axis is that of the individual mAbs.

Table 1: Characteristics of the antibodies described in this study. VH and VL % identity refers to V gene identity compared to germline (IMGT).

mAb	Blood sample date	VH (% identity)	HCDR3 Lenght	HCDR3 sequence	VL (% identity)	LCDR3 sequence	SARS-CoV	SARS-CoV-2	Specifcity
S110	2004	VH3-30 (96.88)	18	AKDRFQFARSWYGDYFDY	VK2-30 (96.60)	MQGTHWPPT	+	+	RBD/non-RBD
S124	2004	VH2-26 (98.28)	17	ARINTAAYDYDSTTFDI	VK1-39 (98.57)	QQSYSTPPT	+	+	RBD
S109	2004	VH3-23 (93.75)	19	ARLESATQPLGYYFYGMDV	VL3-25 (97.85)	HSADISATSWV	+	-	RBD
S111	2004	VH3-30 (95.14)	16	ARDIRHLIVVVSDMDV	VK2-30 (98.30)	MQGTHWPPT	+	-	RBD
S127	2004	VH3-30 (96.53)	18	AKDLFGYCRSTSCESLDD	VK1-9 (98.92)	QQLNNYPLT	+	-	RBD
S215	2004	VH3-30 (90.28))	16	ARETRHYSHGLNWFDP	VK3-15 (98.92)	QQYNNWPTT	+	-	RBD
S217	2004	VH3-49 (95.58)	8	SWIHRIVS	VK1-33 (98.21)	QQYDNLPYT	+	-	RBD
S218	2004	VH3-30 (93.40)	16	ARDVKGHIVVMTSLDY	VK2-30 (97.62)	MQGTHWPPT	+	-	RBD
S219	2004	VH1-58(92.01)	18	AAEMATIQNYYYYYGMDV	VK1-39 (95.34)	QQSYSTPPT	+	-	RBD
S222	2006	VH1-2 (91.67)	15	ARGDVPVGTGWVFDF	VK1-39 (92.47)	QQSLSMVT	+	-	RBD
S223	2006	VH3-30 (95.14)	19	ATVSVEGYTSGWYLGTLDF	VK3-15 (98.21)	QQYNNWPGT	+	-	RBD
S224	2006	VH1-18 (90.97)	15	ARQSHSTRGGWHFSP	VK1-39 (95.70)	QQSYSVPYT	+	-	RBD
S225	2006	VH3-9 (96.18)	20	AKDISLVFWSVNPPRNGMDV	VK1-39 (98.57)	QQSYSSPLT	+	-	RBD
S226	2006	VH3-30 (89.61)	18	ARDSSWQSTGWPINWFDR	VK3-11 (96.11)	QQRSNWPPT	+	-	RBD
S227	2006	VH3-23 (95.14)	12	ASPLRNYGDLLY	VK1-5 (96.06)	QQYNSYSWT	+	-	RBD
S228	2006	VH3-30 (96.53)	16	ARDLQMRVVVVSNFDY	VK2D-30 (99.32)	MQATHWPPT	+	-	RBD
S230	2006	VH3-30 (90.97)	20	VTQRDNSRDYFPHYFHDMDV	VK2-30 (97.62)	MQGSHWPPT	+	-	RBD
S231	2006	VH3-30 (90.62)	17	ARDDNLDRHWPLRLGGY	VK2-30 (94.56)	MQGAHWPPT	+	-	RBD
S237	2006	VH3-21 (96.53)	11	ARGFERYYFDS	VL1-44 (96.84)	VAWDDILNAVV	+	-	RBD
S309	2013	VH1-18 (97.22)	20	ARDYTRGAWFGESLIGGFDN	VK3-20 (97.52)	QQHDTSLT	+	+	RBD
S315	2013	VH3-7 (97.92)	17	ARDLWWNDQAHYYGMDV	VL3-25 (97.57)	QSADSSGTV	+	+	RBD
S303	2013	VH3-23 (90.28)	17	ARERDDIFPMGLNAFDI	VK1-5 (97.49)	QQYDTYSWT	+	+	RBD
S304	2013	VH3-13 (97.89)	14	ARGDSSGYYYYFDY	VK1-39 (93.55)	QQSYVSPTYT	+	+	RBD
S306	2013	VH1-18 (95.49)	16	ASDYFDSSGYYHSFDY	VK3-11 (98.92)	QQRSNWPPGCS	+	+	non-RBD
S310	2013	VH1-69 (92.71)	19	ATRTYDSSGYRPYYYGLDV	VL2-23 (97.57)	CSYAGSDTVI	+	+	non-RBD

Table 2. CryoEM data collection and refinement statistics.

	SARS-CoV-2 S + S309 (closed)	SARS-CoV-2 S + S309 (one S^B open)
Data collection and processing		
Magnification	130,000	130,000
Voltage (kV)	300	300
Electron exposure ($e^-/Å^2$)	70	70
Defocus range (μm)	0.5-3.0	0.5-3.0
Pixel size (Å)	0.525	0.525
Symmetry imposed	C3	C1
Final particle images (no.)	168,449	119,608
Map resolution (Å)	3.3	3.7
FSC threshold	0.143	0.143
Map sharpening *B* factor ($Å^2$)	-91	-69
Validation		
MolProbity score	0.91	
Clashscore	0.9	
Poor rotamers (%)	0.1	
Ramachandran plot		
Favored (%)	97.24	
Allowed (%)	99.91	
Disallowed (%)	0.09	
EMRinger Score	2.58	

Table 3. X-ray data collection and refinement statistics.

	Fab S309
Data collection	
Space group	$P4_12_12$
Cell constants	
a,b,c (Å)	132.6, 132.6, 301.2
α,β,γ (˚)	90, 90, 90
Wavelength (Å)	0.9812
Resolution (Å)	68.6 - 3.3 (3.48 - 3.30)
Rmerge	18 (75)
$I/\sigma(I)$	13.2 (2)
CC(1/2)	99.0 (33)
Completeness (%)	99.4 (99.0)
Redundancy	12
Refinement	
Resolution (Å)	68.6 - 3.3
Unique reflections	41,395
Rwork/Rfree (%)	20.5 / 23.8
Number of protein atoms	8,347
Number of water atoms	0
R.m.s.d. bond lengths (Å)	0.06
R.m.s.d. bond angles (˚)	1.45
Favored Ramachandran residues (%)	96
Allowed Ramachandran residues (%)	3.54
Disallowed Ramachandran residues (%)	0.46

[1]Numbers in parentheses refer to outer resolution shell